Dalton Transactions

ROYAL SOCIETY OF CHEMISTRY

PAPER

View Article Online
View Journal | View Issue



Cite this: *Dalton Trans.*, 2026, **55**, 611

# Tuning birefringence in alkaline-earth metal oxyhalides through diverse mixed-cation coordination architectures

Shenghong Zeng,†[a,b] Mayinuer Maimaiti,†[a,b] Jinche Wu,[b] Tingwen Han,[b] Hui Chai,*[a] Fangfang Zhang *[a,b] and Min Zhang *[a,b]

Received 1st November 2025,
Accepted 2nd December 2025

DOI: 10.1039/d5dt02624e

rsc.li/dalton

A series of new alkali-earth metal complex oxyhalides, $Ba_5Pb_4O_4Br_{10}$ ($4PbO{\cdot}5BaBr_2$), $Ba_2CdSe_2O_6Cl_2$ ($BaCdSe_2O_6{\cdot}BaCl_2$) and $BaCdSeO_3Br_2$ ($CdSeO_3{\cdot}BaBr_2$) have been synthesized by a high-temperature solution method. These compounds exhibit layered structures composed of polyhedra in various configurations, along with distinct symmetry, bonding modes, and cation coordination orientations. Further investigations indicate that the structural variations observed in these materials arise from the structure-directing effect of cations with different sizes. Additionally, this work reports their crystal structures, thermogravimetric analysis, infrared spectroscopy, UV-Vis-NIR diffuse reflectance spectroscopy, scanning electron microscopy/energy dispersive analysis by X-ray and electronic band structures. These new mixed-cation oxyhalide materials feature rich chemical and structural diversity as well as enhanced environmental stability, thus offering important material options for the development of infrared optical devices.



## 1. Introduction

In the vast field of materials science, the design and preparation of new inorganic functional crystals has always been a key driving force behind scientific and technological progress.[1–3] However, crystal synthesis is time-consuming and fraught with challenges.[4] Inorganic functional crystals are widely used in lasers, semiconductors, optoelectronics and other field.[5,6] With technological advancement and growing demands, traditional laser crystals have gradually failed to meet the requirements.[7] Consequently, researchers have conducted extensive and in-depth studies in this field. Through relentless efforts, numerous high-performance crystalline materials have been successfully synthesized. Functional crystals for optical applications can be classified by their transparency bands into deep ultraviolet, ultraviolet, visible light, near-infrared, and mid- to far-infrared crystals. Research on ultraviolet crystal materials primarily focuses on borate system.[8] As an important branch of infrared materials, mid- to far-infrared materials have exhibited great application potential in many frontier scientific and technological fields owing to their unique optical properties.[9,10] Over the past decades, research on infrared optical materials has still focused mainly on non-oxide systems.[11] such as chalcogenides,[12,13] phosphides[14] and selenides.[15] These materials dominate in thermal imaging, infrared sensing, and laser transmission, and related fields due to their wide infrared transmission range (3–5 and 8–14 μm), low phonon energy, and high nonlinear optical properties. Nevertheless, they still face some key challenges, including multi-phonon absorption, difficulty in adjusting the balance of band gap and nonlinear optical effects, challenges in growing large crystals, and poor chemical stability.[16,17] Thus, the development of high-performance infrared functional crystals remains a critical research focus.

In recent years, with researchers unremitting exploration, significant breakthroughs have been made in the field of infrared optical materials. The successful development of a series of high-performance heavy metal oxyhalide crystals has injected new vitality into the infrared optical material system.[18–24] By leveraging the synergistic effect of heavy metal elements (*e.g.*, Pb, Ba, Bi, Sn, Te) with halogen group elements (Cl, Br, I) and oxygen, these novel crystal materials exhibit the comprehensive performance advantages that traditional chalcogenides are difficult to achieve.[25] Studies have demonstrated that such heavy metal oxyhalide crystals not only inherit the wide-band transmission characteristics of oxide system, but also significantly enhance the chemical stability of the materials through unique chemical bonding modes. Notably, by precisely regulating the key structural units such as M–O–X (M = Pb, Ba, Bi, Sn, Te; X = Cl, Br, I), researchers have

[a]*State Key Laboratory of Chemistry and Utilization of Carbon-Based Energy Resources, College of Chemistry, Xinjiang University, Urumqi 830017, PR China. E-mail: hchchh@sina.com, ffzhang@ms.xjb.ac.cn, zhangmin@ms.xjb.ac.cn*
[b]*Research Center for Crystal Materials, CAS Key Laboratory of Functional Materials and Devices for Special Environmental Conditions, Xinjiang Technical Institute of Physics & Chemistry, CAS, 40-1 South Beijing Road, Urumqi 830011, PR China*
†These authors contributed equally to this work.

successfully achieved effective modulation of the phonon energy of the material, thereby expanding their transmission performance in the mid- to far-infrared band.[26–29] These innovative achievements not only enrich the material system of infrared optical crystals, but also provide a new material basis for the development of high-performance infrared optical devices.

With the deepening of research, the mixed-cation strategy is expected to be an effective approach to further enhancing the chemical and structural diversity of heavy metal oxyhalide crystals.[30] Recently, a series of mixed-cation oxyhalide system compounds have been designed and synthesized.[22,27,31–35] Compared with single-metal oxyhalide compounds like $Pb_{17}O_8Cl_{18}$,[19] $Pb_{18}O_8Cl_{15}I_5$,[26] $Pb_{13}O_6Cl_{14}Br_{10}$, $Pb_{13}O_6Cl_7Br_7$, $Pb_{13}O_6Cl_9Br_5$,[11] $Sn_{14}O_{11}Br_6$,[36] and $Sb_5O_7I$, mixed-cation oxyhalides usually show a broad infrared (IR) transparency range (*e.g.*, $CdPbOCl_2$:[37] 1.4–18.0 μm) and larger optical band gap (*e.g.*, $Cd_2TeO_3Cl_2$:[38] 4.25 eV, $CdPb_2Te_3O_8Cl_2$:[23] 3.89 eV, $BaLiTe_2O_5Cl$:[39] 4.25 eV). In addition, the system is likely to include compounds with large birefringence in the infrared band. For example, the birefringence of alkali metal antimony (III) oxyhalide $Rb_2Sb_2OCl_6$ [27] reaches 0.191@550 nm, which is larger than the birefringence value of the oxyhalide crystal material obtained so far. The exploration of new mixed-cation materials with enhanced optical performances is still highly anticipated yet challenging.[40]

Inspired by the above ideas, we have focused extensive attention on the mixed-cation heavy oxyhalides system, and three new alkali-earth metal complex oxyhalides, $Ba_5Pb_4O_4Br_{10}$ ($4PbO{\cdot}5BaBr_2$), $Ba_2CdSe_2O_6Cl_2$ ($BaCdSe_2O_6{\cdot}BaCl_2$) and $BaCdSeO_3Br_2$ ($CdSeO_3{\cdot}BaBr_2$), have been successfully synthesized by a high-temperature melting method. Interestingly, $Ba_5Pb_4O_4Br_{10}$ contains $[Pb_4Ba_4O_4]^{8+}$ species constructed by four $[OBaPb_3]$ oxocentered heterometallic tetrahedra, compounds $Ba_2CdSe_2O_6Cl_2$ and $BaCdSeO_3Br_2$ both have isolated $[SeO_3]$ units, and the cations in the structure show a variety of coordination environment modes. Herein, the great research significance on the structural, optical, thermal, and electronic properties of the title compounds were systematically investigated for their great research significance, which provides a new direction for further exploration and design of mid-infrared functional materials.

## 2. Results and discussion

### 2.1. Structural description of $Ba_5Pb_4O_4Br_{10}$

$Ba_5Pb_4O_4Br_{10}$ crystallizes in the *P*4/*n* (no. 85) space group belonging to the tetragonal system. The energy dispersive X-ray spectroscopy (EDS) spectrum confirms the presence and uniform distribution of Ba, Pb, O, and Br elements in the crystal (Fig. S1). Its asymmetric units contain two, one, one, and four crystallographically independent Ba, Pb, O, and Br atoms respectively. The crystallographic data and atomic coordinates, equivalent isotropic displacement parameters, selected bond lengths, and selected bond angles are listed in Tables S1 and S2 in the SI, respectively. As shown in Fig. 1a and b, the crystal structure of $Ba_5Pb_4O_4Br_{10}$ can be regarded as a relatively covalent $[Pb_4Ba_4O_4]^{8+}$ species partitioned by ionically bonded Ba and Br atoms. The $[Pb_4Ba_4O_4]^{8+}$ species are constructed by four $[OPb_3Ba]$ oxocentered heterometallic tetrahedra (Fig. 1c and d). It should be noted that, the oxocentered $[OPb_4]$ tetrahedron in most lead oxyhalides is often used to describe the crystal structure. However, when the $Pb^{2+}$ cations in the $[OPb_4]$ oxocentered tetrahedron are replaced by other atoms (Cd, Ba, Sb), various oxocentered heterometallic $[OPb_nA_{4-n}]$ tetrahedral structures are formed (Table S3).

In addition, the Ba atoms exhibit two kinds of different coordination modes, $[BaOBr_7]$ and $[BaBr_9]$ polyhedra (Fig. 1e and f), with the bond lengths ranging from 2.536 Å–3.6466 Å

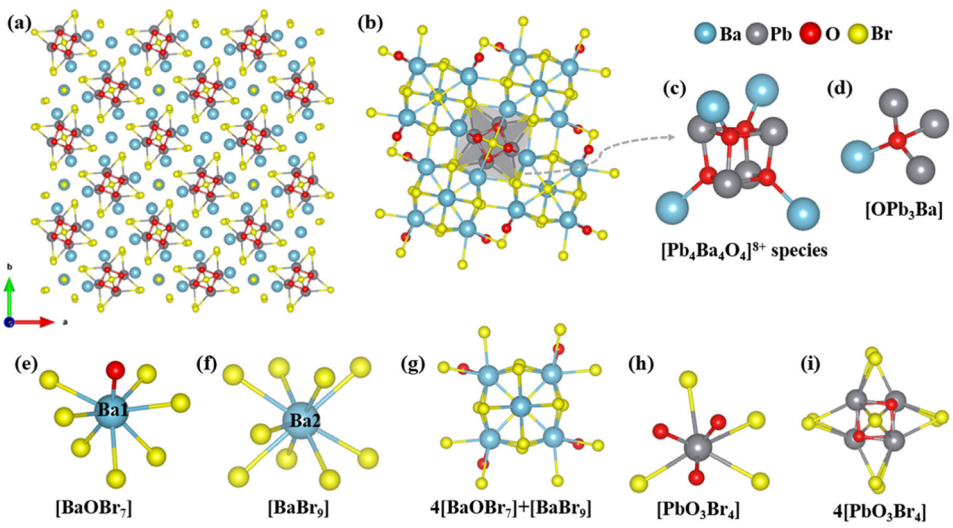


**Fig. 1** (a) Crystal structure of $Ba_5Pb_4O_4Br_{10}$; (b) chemical bonding in one unit cell; (c) $[Pb_4Ba_4O_4]^{8+}$ species; (d) $[OPb_3Ba]$ tetrahedra; coordination modes of Ba and Pb atoms (e, f, g, h, i).

 

and 3.4143 Å–3.6114 Å, respectively. Four [$BaOBr_7$] units and one [$BaBr_9$] unit are connected to forma [Ba–O–Br] unit by sharing Br atoms (Fig. 1e–g). The Pb atom is coordinated to three O atoms and four Br atoms, forming a [$PbO_3Br_4$] unit with bond distances of 2.2640(5)–3.6405 Å. Subsequently, four [$PbO_3Br_4$] groups connect with each other by sharing O and Br atoms to form a [Pb–O–Br] cluster (resembling a "quadrangle") (Fig. 1h and i), and these [Pb–O–Br] clusters are inserted into the [Ba–O–Br] units to construct 3D frameworks. For the overall structure of $Ba_5Pb_4O_4Br_{10}$, it features a complicated 3D network composed of ionic salt $BaBr_2$ inserted into covalent $[Pb_4Ba_4O_4]^{8+}$ species. The chemical bonds in one unit cell, which is representive of the entire structure due to the high symmetry of the tetragonal system, are depicted in Fig. 1b.

The bond valence sums (BVS) of each atom in $Ba_5Pb_4O_4Br_{10}$ were calculated and listed in Table S4 in the SI. We can see from Table S2 that the BVS values of the Pb, Ba, O, and Br atoms are 2.32, 1.71–2.42, 2.41, 0.98–1.26, respectively. These valence sums agree with expected oxidation states, which further validates the rationality of the crystal structure analysis.

To further analyze and compare the structural features of lead-containing mixed metal oxyhalides, we surveyed the structural characteristics of such compounds based on the latest version of the ICSD (ICSD-5.3.0). Among the reported mixed metal oxyhalides, nearly all exhibit oxygen-centered fundamental building blocks (FBBs) with general formula [$OPb_nA_{4-n}$], a feature like that of some lead oxyhalide system compounds, which also contain the common [$OPb_4$] unit. We also statistically analyzed the Pb/A–O–Pb/A angles and the corresponding O–Pb/A bond lengths for each oxygen-centered unit in lead-containing mixed metal oxyhalides, as shown in Fig. 2 and Table S5. Basic statistical results indicate that when $Pb^{2+}$ cations in the [$OPb_4$] units are substituted by other metal cations with larger ionic radii, both the average bond lengths and angles change, resulting in distortions of the FBB structures.[41–43]

Observations and statistics of mixed metal oxyhalides show that the oxygen-centered FBBs in the compounds form O–Pb–A frameworks through polymerization in different dimensions. As shown in Table S3, this fully demonstrates the diversity and richness of the structural chemistry of oxyhalide compounds.

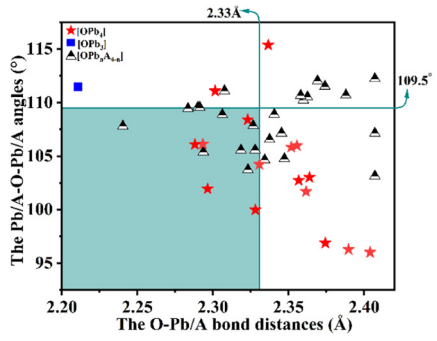


Fig. 2 The statistics of Pb/A–O–Pb/A angles (°) and O–Pb/A bond distances (Å) in the crystal structure of lead heterometallic oxyhalide compounds.

Interestingly, the title compound $Ba_5Pb_4O_4Br_{10}$ exhibits the same FBBs (the isolated [$Pb_4O_4$] cluster formed by four [$PbO_3$] groups) with alkali-earth metal lead(II) oxyhalide compound $Ba_{27}Pb_8O_8Cl_{54}$,[34] but differs in the coordination environment of Ba and Pb atoms. Furthermore, they crystallize in different space groups: $Ba_5Pb_4O_4Br_{10}$ belongs to tetragonal space group $P4/n$ (no. 85), while $Ba_{27}Pb_8O_8Cl_{54}$ belongs to cubic space group $Fm3m$ (no. 225) (Fig. S2). It can be observed that compound $Ba_{27}Pb_8O_8Cl_{54}$ has a higher structural symmetry compared to $Ba_5Pb_4O_4Br_{10}$, which can also be observed from the oxocentered [$OPb_3$] triangle in the isolated [$Pb_4O_4$] cluster. Specifically, the [$OPb_3$] units in $Ba_{27}Pb_8O_8Cl_{54}$ form congruent triangles with, an O–Pb bond length of 2.272 Å and the Pb–O–Pb angles of 99.94°.

### 2.2. Structural description of $Ba_2CdSe_2O_6Cl_2$

$Ba_2CdSe_2O_6Cl_2$ crystallizes in the space group *Pnma* (no. 62) of the orthorhombic crystal system. The asymmetric unit of $Ba_2CdSe_2O_6Cl_2$ consists of one, one, one, two, and one crystallographic independent Ba, Cd, Se, O, and Cl atoms, respectively (Table S4 in the SI). The existence of compositional elements, namely, Ba, Cd, Se, O, and Cl was verified by energy dispersive X-ray spectroscopy (EDS) (Fig. S1). The crystallographic data and atomic coordinates, equivalent isotropic displacement parameters, selected bond lengths, and selected bond angles are listed in Tables S1 and S6 in the SI, respectively. A diagram showing the coordination around the cations is given in Fig. 3. Ba is bonded to seven O and three Cl atoms to form a [$BaO_7Cl_3$] polyhedral unit, the bond lengths range of Ba–O and Ba–Cl is 3.2533(12)–3.3448(8) Å, 2.666(4)–3.1029(18) Å, respectively, and the [$BaO_7Cl_3$] units are connected with each other *via* corner-sharing to form $^1_\infty[BaO_5Cl_2]$ chains (Fig. 3c), these chains are further connected by atom-sharing to form [Ba–O–Cl] layers along *a*-axis (Fig. 3e). The Cd-atom coordinate four O and two Cl, forming a [$CdO_4Cl_2$] octahedron unit with the bond lengths $d$(Cd–Cl) = 2.6268(11) Å and $d$(Cd–O) = 2.279(2) Å (Fig. 3a), there the $Cd^{2+}$ cation has a symmetric coordination with the formation of bonds. The Se atoms are coordinated with three oxygen atoms to form isolated [$SeO_3$] units ([$SeO_3$] pseudo-layers) with $d$(Se–O) = 1.670(4)–1.712(2) Å (Fig. 3d). The [$CdO_4Cl_2$] octahedron units are combined with [Ba–O–Cl] layers to form [Ba–Cd–O–Cl] layers (Fig. 3f). The [$SeO_3$] pseudo-layers are interconnected with [Ba–Cd–O–Cl] layers to give the final three-dimensional (3D) structure with mixed cationic layers in $Ba_2CdSe_2O_6Cl_2$ (Fig. 3g), and the structure is similar to "sandwich" (Fig. 3h).

Bond-valence sum (BVSs) calculations yield the following reasonable values; 2.05 for Ba, 2.07 for Cd, 4.08 for Se, 2.12 for O (1), 2.05 for O (2), 0.88 for Cl (Table S4 in the SI), those are in agreement with the expected oxidation states of +2, +2, +4, −2, and −1, respectively, thus verifying the reasonability of the crystal structure.

### 2.3. Structural description of $BaCdSeO_3Br_2$

$BaCdSeO_3Br_2$ crystallizes in the orthorhombic crystal system with a space group of *Pnma* (no. 62). In its asymmetric unit,

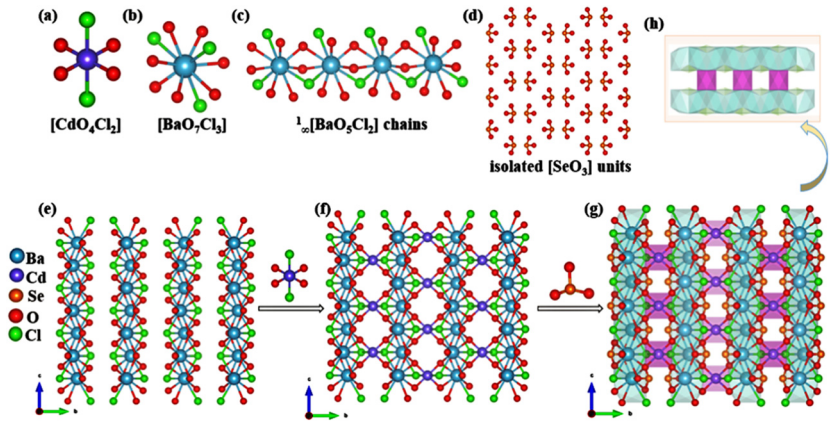


**Fig. 3** Crystal structure of $Ba_2CdSe_2O_6Cl_2$. The coordination modes of (a and b) Cd and Ba, (c) the formed $[BaO_5Cl_2]$ chains, (d) the formed $[SeO_3]$ pseudo-layers by isolated $[SeO_3]$ units, (d) the formed [Ba–O–Br] layers viewed from the *a* direction, (f) the structure of $[CdO_5Cl_2]$ units interconnected with layers along *a* direction, (g), and (g, h) the three-dimensional structure of $Ba_2CdSe_2O_6Cl_2$ with mixed cationic layers (similar to the "sandwich" structure).

there are one crystallographically unique Ba atom, one Cd atom, one Se atom, two O atoms, and two Br atoms (Table S4). Ba is bonded to six O and four Br atoms to form a $[BaO_6Br_4]$ polyhedral unit with the bond lengths $d$(Ba–Br) = 3.5480(6)–3.7326(8) Å and $d$(Ba–O) = 2.773(2)–3.0907(16) Å (Fig. 4a), and the $[BaO_6Br_4]$ units are further linked with each other and arranged along the *c*-axis in the *ab* plane to form $^1_\infty[BaO_4Br_3]$ chains (Fig. 4d). Cd is coordinated to three O and four Br atoms, forming $[CdO_3Br_4]$ octahedral unit with $d$(Cd–Br) = 2.6314(6)–2.9403(7) Å and $d$(Cd–O) = 2.170(3)–2.462(2) Å (Fig. 4b). The Se atoms are coordinated with three oxygen atoms to form isolated $[SeO_3]$ units with $d$(Se–O) = 1.691(3) to 1.694(2) Å (Fig. 4f). Every two $[CdO_3Br_4]$ octahedral units are connected with each other by edge sharing to construct a $[Cd_2O_6Br_6]$ octahedral dimer structure (Fig. 4c and e). The $[Cd_2O_6Br_6]$ dimers are combined with $^1_\infty[BaO_4Br_3]$ chains to form [Ba–Cd–O–Br] layers (Fig. 4g). The $[SeO_3]$ pseudo-layers formed by the isolated units are interconnected with [Ba–Cd–O–Br] layers to give the final three-dimensional (3D) structure with mixed cationic layers in $BaCdSeO_3Br_2$ (Fig. 4h). The existence of compositional elements, namely, Ba, Cd, Se, O, and Br was verified by energy dispersive X-ray spectroscopy (EDS) l (Fig. S1). The calculated bond valence sums (BVSs) (Ba: 1.94, Ba: 2.07, Se: 4.13, O: 2.06–2.10, and Br: 0.88–1.04) (Table S4 in the SI) confirms the rationality of the crystal structure. The detailed information on bond lengths and angles, atomic coordinates and equivalent isotropic displacement parameters is provided in Table S7.

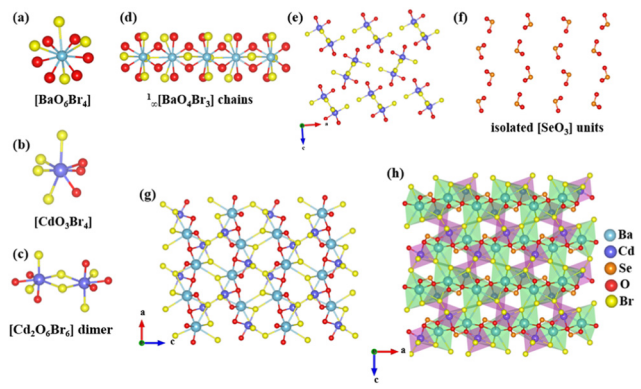


**Fig. 4** Crystal structure of $BaCdSeO_3Br_2$. The coordination modes of (a and b) Ba and Cd, (c) $[Cd_2O_6Br_6]$ dimer, (d) the formed $[BaO_4Br_3]$ chains, (e) the formed $[Cd_2O_6Br_6]$ octahedral dimers viewed from the *b* direction, (f) the formed $[SeO_3]$ pseudo-layers by isolated $[SeO_3]$ units, (g) the structure before the insertion of $[SeO_3]$ pseudo-layer viewed from the *b* directions, and (h) the three-dimensional structure of $BaCdSeO_3Br_2$ with mixed cationic layers.

### 2.4. Thermal stability and optical analysis

The polycrystalline powder samples of $Ba_5Pb_4O_4Br_{10}$, $Ba_2CdSe_2O_6Cl_2$, and $BaCdSeO_3Br_2$ were obtained *via* a high temperature solid-state reaction technique in a closed system for further characterization. The XRD (X-ray diffraction) curves of the powder samples are in good agreement with the simulated patterns calculated from the CIF data, as shown in Fig. 5a–c. However, despite our many attempts, the obtained polycrystalline powder of $BaCdSeO_3Br_2$ still contains small amounts of unknown impurities. The thermal behavior of compounds was characterized by TG–DSC measurement, and their TG–DSC curves are depicted in Fig. 5d–f. During the heating process, one prominent endothermic peak is observed for $Ba_5Pb_4O_4Br_{10}$ and $Ba_2CdSe_2O_6Cl_2$ around 730 and 714 °C, respectively, with slight weight loss at approximately 725 °C and 620 °C, indicating that these two compounds are quite stable. For $BaCdSeO_3Br_2$, two distinct endothermic peaks at ~634 °C (onset at 600 °C) and 727 °C on the heating curve, while continuous weight loss occurs from 453 °C onward as temperature increases.

To further verify the thermal properties of the three compounds, powder XRD measurement were performed on samples before and after melting experiments. The ground

 

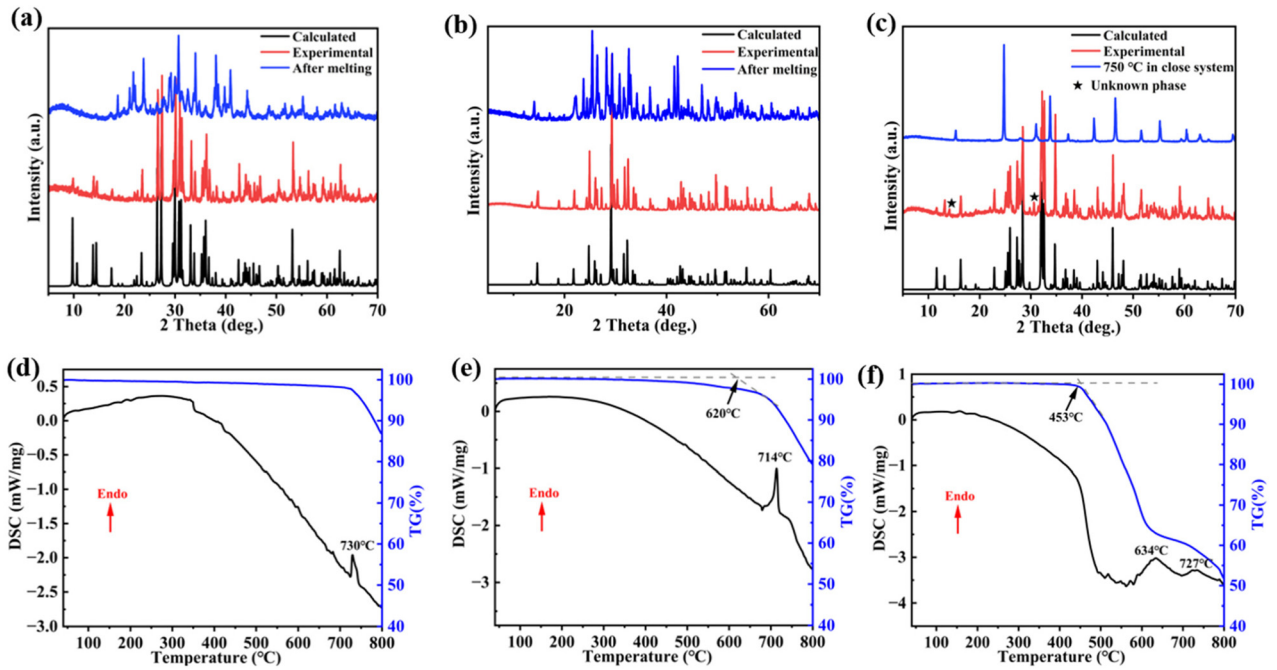


**Fig. 5** The XRD patterns and TG–DSC curves of (a, d) $Ba_5Pb_4O_4Br_{10}$, (b, e) $Ba_2CdSe_2O_6Cl_2$, and (c, f) $BaCdSeO_3Br_2$.

crystallized products were subjected to additional Powder XRD analysis. As depicted in Fig. 5a–c, the fully melt crystallized products of $Ba_5Pb_4O_4Br_{10}$ and $Ba_2CdSe_2O_6Cl_2$ exhibit diffraction patterns different from those of the original pure powders, demonstrating that $Ba_5Pb_4O_4Br_{10}$ and $Ba_2CdSe_2O_6Cl_2$ melt incongruently. For $BaCdSeO_3Br_2$, the sample tends to decompose with increasing temperature. Therefore, the above compounds require the addition of flux during crystal growth, which is consistent with their crystal preparation methods.

The UV-Vis NIR diffuse reflectance spectra of pure phase powder were recorded at room temperature over the wavelength range of 200–2600 nm at room temperature (Fig. 6a–c). Based on the Kubelka–Munk equation, the experimental band-gaps are 3.49 eV, 5.03 eV, and 3.72 eV, respectively. Notably, $Ba_2CdSe_2O_6Cl_2$ has large band gap compared with the currently reported heavy metal oxyhalides. This large band gap is associated with its ionically bonded alkaline-earth metal Ba and the unique structure of the $d^{10}$ transition metal Cd (fully filled 4d orbitals) can effectively suppress the excessive electron cloud polarization, and realize wide-range regulation of the energy band structure *via* orbital hybridization. Additionally, the content of highly electronegative halogens can significantly reduce band dispersion, which is beneficial for band gap enlargement. Furthermore, by comparing the optical properties of some reported mixed-metal oxyhalides listed in Table S8, we found that mixed-anion inorganic compounds containing stereochemically active lone-pair (SCALP) cations (Pb, Bi, Sb, Te, Sn, *etc.*) may reduce the band gap to a certain extent.[44]

The IR spectra were also recorded. The infrared absorption spectra reveal that the absorption peaks of the above compounds concentrated in the range of 400–1000 $cm^{-1}$ (Fig. 6d–f). Specifically, the peaks at approximately 400–600 $cm^{-1}$ are likely attributed to the Pb–O and Cd–O bonds.[45] Additionally, the prominent peaks at 650–850 $cm^{-1}$ can be assigned to Se–O bond vibrations, which is consistent with reported metal selenites.[46] Infrared spectroscopy measurements further confirm that $Ba_5Pb_4O_4Br_{10}$, $Ba_2CdSe_2O_6Cl_2$ and $BaCdSeO_3Br_2$ exhibit no significant absorption in the mid-infrared region.

### 2.5. Theoretical analysis

To explain the intrinsic microscopic mechanism by which electronic structure influences optical properties, first-principles (DFT) calculations using CASTEP software were performed on three compounds. The band structures and densities of states (DOS) were calculated *via* the plane wave pseudopotential method. Based on the generalized gradient approximation (GGA), the calculated band gap of $Ba_5Pb_4O_4Br_{10}$, $Ba_2CdSe_2O_6Cl_2$ and $BaCdSeO_3Br_2$ are 3.637 eV, 4.222 eV and 3.905 eV, respectively (Fig. 7a, b and c). Among these compounds, $Ba_5Pb_4O_4Br_{10}$ and $Ba_2CdSe_2O_6Cl_2$ are direct band gap compounds because their valence band maximum (VBM) and the conduction band minima (CBM) are located at the same *k*-points. In contrast, the VBM and CBM of $BaCdSeO_3Br_2$ are not at the same position in *k*-space (Brillouin zone), indicating it is an indirect band gap compound. The total density of states (DOS) and the partial density of states (PDOS) projected onto the constituent atoms of the three compounds are shown in Fig. 7d–f. For $Ba_5Pb_4O_4Br_{10}$, the Ba 6s, Pb 6p, O 2p and Br 4s orbitals are the primary contributors to the conduction bands (CBs) in the range of 0 to 15 eV, the other orbitals make relatively minor contributions. The Ba 5p, Pb 5d, O 2p and Br

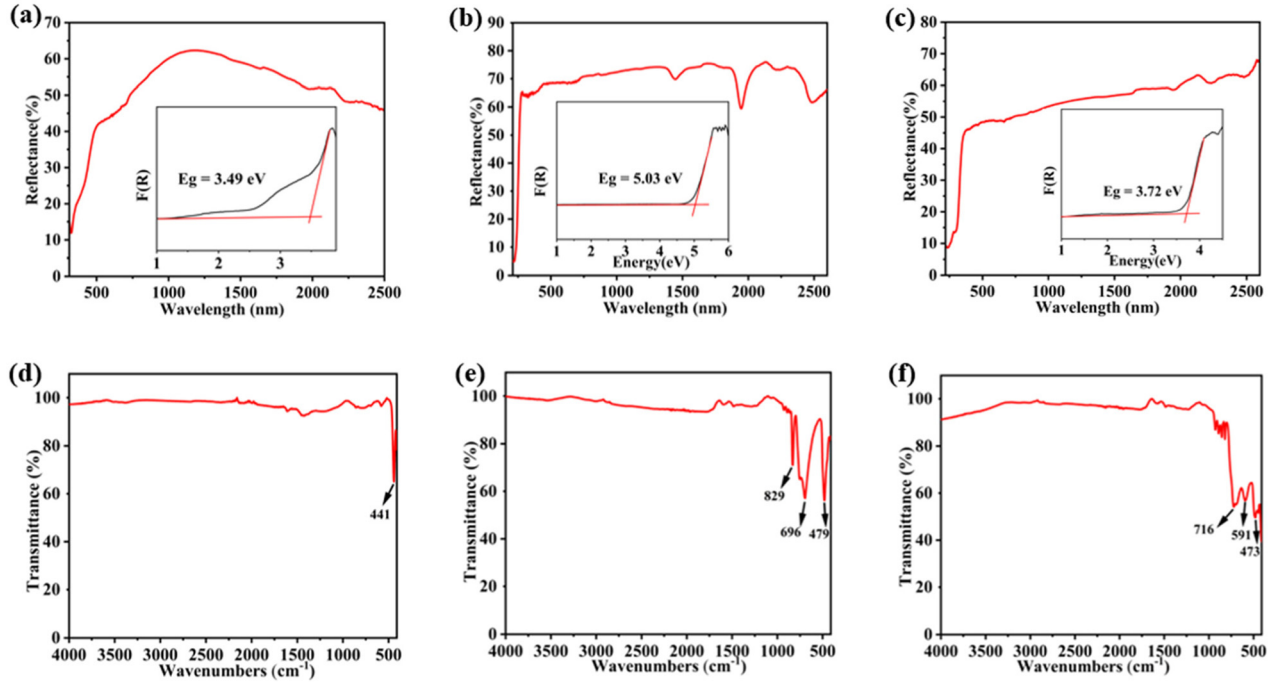


**Fig. 6** The UV-Vis-NIR diffuse reflectance spectra and IR spectra of (a, d) $Ba_5Pb_4O_4Br_{10}$, (b, e) $Ba_2CdSe_2O_6Cl_2$, and (c, f) $BaCdSeO_3Br_2$.

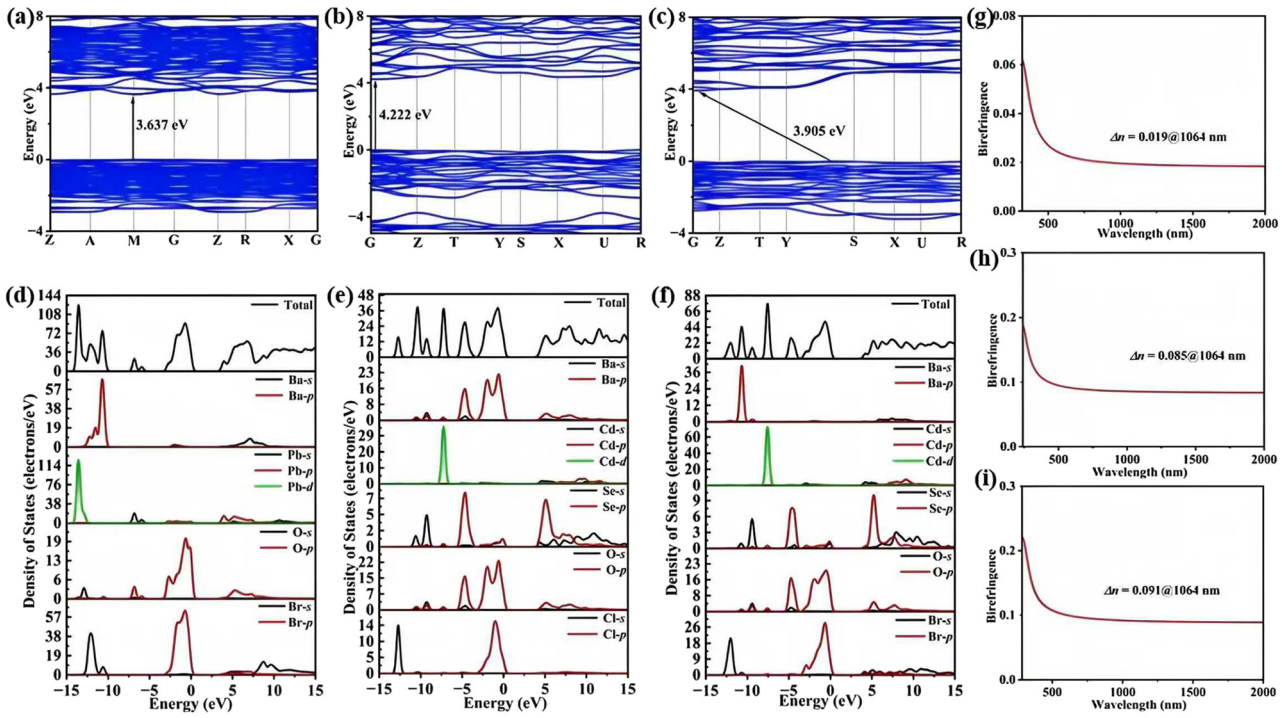


**Fig. 7** (a, b, c) Band structure; (d, e, f) total and partial density of states; (g, h, i) calculated birefringence of $Ba_5Pb_4O_4Br_{10}$, $Ba_2CdSe_2O_6Cl_2$ and $BaCdSeO_3Br_2$, respectively.

4s 4p orbitals dominate the valence bands (VBs) region between 0 and −15 eV. For $Ba_2CdSe_2O_6Cl_2$, the top of the VBs is primarily occupied by Ba 5p, Cd 4d, Se 4p, O 2p and Cl 3p orbitals, whereas the bottom of the CBs is mainly determined by Se 4s 4p and O 2p orbitals. For $BaCdSeO_3Br_2$, Se 4p, O 2p and Br 4p orbitals predominantly contribute to the top of VBs near the Fermi level, whereas the bottom of CBs mainly comprises Se 4p and O 2p orbitals.

 

Based on DFT, the refractive indices of $Ba_5Pb_4O_4Br_{10}$, $Ba_2CdSe_2O_6Cl_2$ and $BaCdSeO_3Br_2$ were calculated, and the theoretical refractive index curves are illustrated in Fig. 7g–i. As shown, the calculated birefringence values of the three compounds at 1064 nm is 0.019, 0.085 and 0.091, respectively. Among them, the smaller birefringence of $Ba_5Pb_4O_4Br_{10}$ can be attributed to the inherent weak optical anisotropy of its structure. To further accurately understand and analyze the origin of birefringence in these three compounds, the contribution of each structural unit was calculated *via* the response electron distribution anisotropy (REDA) method. This method has been widely used to characterize optical anisotropy in ultraviolet and infrared optical crystals. Given that the optical anisotropy of crystals is closely related to their internal electronic structure, bonding electron density differential ($\Delta\rho$) was introduced to characterize their optical anisotropy. In $Ba_5Pb_4O_4Br_{10}$, the $[BaOBr_7]$ units exhibit the highest optical anisotropy ($\Delta\rho$ = 0.000502, 69.48%), while the $[BaBr_9]$ units exhibit the lowest ($\Delta\rho$ = 0.000093, 12.81%). For $Ba_2CdSe_2O_6Cl_2$, the calculated results show that the $[SeO_3]$ units contribute the most to optical anisotropy ($\Delta\rho$ = 0.002106, 44.52%), followed by the $[BaO_7Cl_3]$ units ($\Delta\rho$ = 0.001614, 34.12%), and the $[CdO_4Cl_2]$ units contribute the least ($\Delta\rho$ = 0.001010, 21.36%). Furthermore, for $BaCdSeO_3Br_2$, the $[BaO_6Br_4]$ units exhibit the highest optical anisotropy ($\Delta\rho$ = 0.003930, 43.34%), followed by the $[SeO_3]$ units ($\Delta\rho$ = 0.003448, 38.02%), and the $[CdO_3Br_4]$ units exhibit the lowest ($\Delta\rho$ = 0.001690, 18.64%) (Table S9).

## 3. Conclusions

In summary, this study employed mixed-cation strategy to successfully introduce the alkaline-earth metal cation (barium) into the heavy-metal oxyhalide system, and three novel alkaline-earth metal complex oxyhalides, $Ba_5Pb_4O_4Br_{10}$, $Ba_2CdSe_2O_6Cl_2$, and $BaCdSeO_3Br_2$, were synthesized *via* the high-temperature solution method. A systematic investigation was conducted on the single crystal structures, optical properties, and electronic structures of these three compounds through a combination of experimental characterization and theoretical calculations. The aforementioned compounds exhibit structural frameworks with different dimensions and a rich structural compositional diversity. $Ba_5Pb_4O_4Br_{10}$ features zero-dimensional $[Pb_4Ba_4O_4]^{8+}$ structural units. Both $Ba_2CdSe_2O_6Cl_2$ and $BaCdSeO_3Br_2$ contain $[SeO_3]$ pseudo-layers composed of isolated $[SeO_3]$ units. These structural characteristics are expected to expand the structural and functional diversity of heavy metal oxyhalides and offer valuable references for the exploration of novel infrared optical materials.

## Conflicts of interest

There are no conflicts to declare.

## Data availability

The authors confirm that the data supporting the findings of this study are available within the article [and/or its supplementary information (SI)]. Supplementary information is available. See DOI: https://doi.org/10.1039/d5dt02624e.

CCDC 2496401–2496403 contain the supplementary crystallographic data for this paper.[47a–c]

## Acknowledgements

This work was supported by the Natural Science Foundation of Xinjiang Uygur Autonomous Region (2022D01E89), the Xinjiang Tianshan Talent Program (2022TSYCCX0072), the Tianshan Innovation Team (2022TSYCTD0005).

## References

1 (*a*) N. Savage, *Nat. Photonics*, 2007, **1**, 83–85; (*b*) F. Zhang, X. Chen, M. Zhang, W. Jin, S. Han, Z. Yang and S. Pan, *Light: Sci. Appl.*, 2022, **11**, 252; (*c*) Y. Wu, C. Cui, G. Han, Y. Wang, F. Li, F. Zhang, Z. Yang and S. Pan, *Adv. Mater.*, 2025, e10775.

2 (*a*) K. M. Ok, E. O. Chi and P. S. Halasyamani, *Chem. Soc. Rev.*, 2006, **35**, 710–717; (*b*) M. Wu, E. Tikhonov, A. Tudi, I. Kruglov, X. Hou, C. Xie, S. Pan and Z. Yang, *Adv. Mater.*, 2023, **35**, 2300848.

3 (*a*) J. K. Harada, N. Charles, K. R. Poeppelmeier and J. M. Rondinelli, *Adv. Mater.*, 2019, **31**, 1805295; (*b*) B. Chen, S. An, X. Hou and S. Pan, *Coord. Chem. Rev.*, 2026, **547**, 217106.

4 (*a*) Z. Yan, J. Fan, S. Pan and M. Zhang, *Chem. Soc. Rev.*, 2024, **53**, 6568–6599; (*b*) Y. Kong, G. Zheng, Y. Du, J. Li and S. Pan, *Coord. Chem. Rev.*, 2025, **533**, 216524.

5 (*a*) J. Sun, T. Abudouwufu, C. Jin, Z. Guo and M. Zhang, *Inorg. Chem.*, 2022, **61**, 688–692; (*b*) F. Zhang, Z. Chen, C. Cui, Z. Yang, M. Mutailipu, F. Li, X. Hou, X. Long and S. Pan, *ArXiv*, 2025, preprint, arXiv:2503.05019, DOI: 10.48550/2503.05019.

6 (*a*) L. Zhang, M. Zhang, L. Wang, X. Chen, J. Jiao, S. Pan, G. Tang, X. Zhang, Z. Chen and X. Zhang, *Opt. Mater.*, 2020, **107**, 110088; (*b*) W. Zhang, X. Hou, S. Han and S. Pan, *Coord. Chem. Rev.*, 2024, **505**, 215664.

7 (*a*) M. Zhang, X. Su, S. Pan, Z. Wang, H. Zhang, Z. Yang, B. Zhang, L. Dong, Y. Wang, F. Zhang and Y. Yang, *J. Phys. Chem. C*, 2014, **118**, 11849–11856; (*b*) H. Wang, R. An, Z. Yang and S. Pan, *Adv. Funct. Mater.*, 2025, **35**, 2504210.

8 (*a*) B. Zhang, G. Shi, Z. Yang, F. Zhang and S. Pan, *Angew. Chem., Int. Ed.*, 2017, **56**, 3916–3919; (*b*) H. Su, J. Jiao, S. Wang, D. An and M. Zhang, *Dalton Trans.*, 2024, **53**, 932–937; (*c*) Z. Yan, J. Fan, D. Chu, Z. Yang, J. Lu, S. Pan and M. Zhang, *Inorg. Chem.*, 2024, **63**, 16461–16469; (*d*) J. Jiao, M. Zhang and S. Pan, *Angew. Chem., Int. Ed.*, 2023, **62**, e202217037; (*e*) H. Su, Z. Yan, X. Hou and M. Zhang,

*Chin. J. Struct. Chem.*, 2023, **42**, 100027; (*f*) M. Mutailipu, M. Zhang, H. Wu, Z. Yang, Y. Shen, J. Sun and S. Pan, *Nat. Commun.*, 2018, **9**, 3089; (*g*) X. Wang, Y. Wang, B. Zhang, F. Zhang, Z. Yang and S. Pan, *Angew. Chem., Int. Ed.*, 2017, **56**, 14119–14123; (*h*) M. Mutailipu, M. Zhang, B. Zhang, L. Wang, Z. Yang, X. Zhou and S. Pan, *Angew. Chem., Int. Ed.*, 2018, **57**, 6095–6099; (*i*) G. Shi, Y. Wang, F. Zhang, B. Zhang, Z. Yang, X. Hou, S. Pan and K. R. Poeppelmeier, *J. Am. Chem. Soc.*, 2017, **139**, 10645–10648; (*j*) J. Huang, C. Zhang, and A. Abudurusuli, *Coord. Chem. Rev.*, 2025, **536**, 216632; (*k*) Z. Yan, D. Chu, M. Zhang, Z. Yang and S. Pan, *Adv. Opt. Mater.*, 2023, **11**, 2202353; (*l*) S. Guo, W. Zhang, M. Zhang, Z. Yang and S. Pan, *Inorg. Chem.*, 2021, **60**, 883–891; (*m*) T. Abudouwufu, M. Zhang, S. Cheng, H. Zeng, Z. Yang and S. Pan, *Chem. Mater.*, 2020, **32**, 3608–3614; (*n*) M. Zhang, D. An, C. Hu, X. Chen, Z. Yang and S. Pan, *J. Am. Chem. Soc.*, 2019, **141**, 3258–3264.

9 (*a*) C. Hu, B. Zhang, B.-H. Lei, S. Pan and Z. Yang, *ACS Appl. Mater. Interfaces*, 2018, **10**, 26413–26421; (*b*) L. Wang, D. Chu, M. Mutailipu, H. Wang, J. Lu, Z. Chen, J. Li and S. Pan, *Adv. Funct. Mater.*, 2025, e15259.

10 (*a*) L. I. Isaenko and A. P. Yelisseyev, *Semicond. Sci. Technol.*, 2016, **31**, 123001; (*b*) Y. Chu, H. Wang, Q. Chen, X. Su, Z. Chen, Z. Yang, J. Li and S. Pan, *Adv. Funct. Mater.*, 2024, **34**, 2314933.

11 X. Chen, H. Jo and K. M. Ok, *Angew. Chem., Int. Ed.*, 2020, **59**, 7514–7520.

12 (*a*) J. Petit, M. Bejet and J.-C. Daux, *Mater. Chem. Phys.*, 2010, **119**, 1–3; (*b*) Y. Yun, M. Wu, Z. Yang, G. Li and S. Pan, *Adv. Sci.*, 2025, **12**, 2417851.

13 N. Dulgheru, M. Gartner, M. Anastasescu, M. Stoica, M. Nicolescu, H. Stroescu, I. Atkinson, V. Bratan, I. Stanculescu, A. Szekeres, P. Terziyska and M. Fabian, *Infrared Phys. Technol.*, 2018, **93**, 260–270.

14 (*a*) G. D. Boyd, E. Buehler and F. G. Storz, *Appl. Phys. Lett.*, 1971, **18**, 301–304; (*b*) Y. Huang, D. Chu, Y. Zhang, C. Xie, G. Li and S. Pan, *Angew. Chem., Int. Ed.*, 2024, **63**, e202406576.

15 G. Airoldi, P. Beucherie and C. Rinaldi, *J. Cryst. Growth*, 1977, **38**, 239–244.

16 (*a*) P. Gong, F. Liang, L. Kang, X. Chen, J. Qin, Y. Wu and Z. Lin, *Coord. Chem. Rev.*, 2019, **380**, 83–102; (*b*) P. Wang, Y. Chu, A. Tudi, C. Xie, Z. Yang, J. Li and S. Pan, *Adv. Sci.*, 2022, **9**, 2106120.

17 (*a*) S. Han, M. Mutailipu, A. Tudi, Z. Yang and S. Pan, *Chem. Mater.*, 2020, **32**, 2172–2179; (*b*) L. Luo, L. Wang, J. Chen, J. Zhou, Z. Yang and S. Pan, *J. Am. Chem. Soc.*, 2022, **144**, 21916–21925.

18 M. Yang, Z.-H. Shi, W.-D. Yao and S.-P. Guo, *Inorg. Chem.*, 2022, **61**, 42–46.

19 H. Zhang, M. Zhang, S. Pan, X. Dong, Z. Yang, X. Hou, Z. Wang, K. B. Chang and K. R. Poeppelmeier, *J. Am. Chem. Soc.*, 2015, **137**, 8360–8363.

20 C. Deng, J. Wang, M. Hu, X. Cui, H. Duan, P. Li and M.-H. Lee, *Nanomaterials*, 2023, **13**, 3037.

21 D. O. Charkin, A. S. Borisov, V. E. Kireev, A. N. Kuznetsov, S. Umedov, E. V. Nazarchuk, V. N. Bocharov and O. I. Siidra, *J. Solid State Chem.*, 2022, **312**, 123277.

22 Z. Yang, C. Hu, M. Mutailipu, Y. Sun, K. Wu, M. Zhang and S. Pan, *J. Mater. Chem. C*, 2018, **6**, 2435–2442.

23 C. Bai, Y. Chu, J. Zhou, L. Wang, L. Luo, S. Pan and J. Li, *Inorg. Chem. Front.*, 2022, **9**, 1023–1030.

24 X. Chen, Q. Jing and K. M. Ok, *Angew. Chem., Int. Ed.*, 2020, **59**, 20712–20712.

25 (*a*) P. S. Halasyamani, *Chem. Mater.*, 2004, **16**, 3586–3592; (*b*) Y.-J. Jia, X. Zhang, Y.-G. Chen, X. Jiang, J.-N. Song, Z. Lin and X.-M. Zhang, *Inorg. Chem.*, 2022, **61**, 15368–15376; (*c*) M. Abudoureheman, L. Wang, X. Zhang, H. Yu, Z. Yang, C. Lei, J. Han and S. Pan, *Inorg. Chem.*, 2015, **54**, 4138–4142; (*d*) H.-S. Ra, K. M. Ok and P. S. Halasyamani, *J. Am. Chem. Soc.*, 2003, **125**, 7764–7765; (*e*) Y. H. Kim, D. W. Lee and K. M. Ok, *Inorg. Chem.*, 2014, **53**, 1250–1256.

26 X. Chen, Q. Jing and K. M. Ok, *Angew. Chem., Int. Ed.*, 2020, **59**, 20323–20327.

27 X.-Y. Li, X. Cheng, C.-L. Hu, B.-X. Li, Z. Zhou, J.-H. Zhang, S. Deng, J.-G. Mao and F. Kong, *Angew. Chem., Int. Ed.*, 2025, **64**, e202501481.

28 X. Chen and K. M. Ok, *Chem. Sci.*, 2022, **13**, 3942–3956.

29 C. Hu, D. Chu, X. Hou, F. Zhang and J. Han, *Inorg. Chem. Front.*, 2024, **11**, 3367–3376.

30 L. Dong, S. Pan, Y. Wang, H. Yu, Q. Bian, Z. Yang, H. Wu and M. Zhang, *CrystEngComm*, 2014, **16**, 5993–5996.

31 X. Chen and K. M. Ok, *Chem. – Asian J.*, 2020, **15**, 3709–3716.

32 K. M. Ok, *Chem. Commun.*, 2019, **55**, 12737–12748.

33 Z. Fan, C. Bai, H. Shi, M. Zhang, B. Zhang, J. Zhang and J. Li, *Dalton Trans.*, 2021, **50**, 14038–14043.

34 P. Ren, Y. Yang and S. Pan, *J. Mol. Struct.*, 2019, **1190**, 23–28.

35 Z. Li, S. Zhang, W. Xing, Z. Lin, J. Yao and Y. Wu, *Dalton Trans.*, 2020, **49**, 3667–3671.

36 Z. Lu, F. Zhang, A. Tudi, Z. Yang, Z. Li and S. Pan, *J. Mater. Chem. C*, 2021, **9**, 7103–7109.

37 C. Bai, B. Cheng, K. Zhang, M. Zhang, S. Pan and J. Li, *Dalton Trans.*, 2021, **50**, 16401–16405.

38 L. Wang, C. Bai, Y. Kong, M. Iqbal, Y. Chu and J. Li, *Dalton Trans.*, 2023, **52**, 16297–16302.

39 T. Wang, Y.-G. Chen, Y. Guo, F. Wang, Q. Song, Y.-J. Jia and X.-M. Zhang, *Dalton Trans.*, 2020, **49**, 4914–4919.

40 J. Yu, B. Zhang, X. Zhang, Y. Wang, K. Wu and M.-H. Lee, *ACS Appl. Mater. Interfaces*, 2020, **12**, 45023–45035.

41 M. Maimaiti, Y. Yan, J. Wu, T. Han, J. Xie and M. Zhang, *Dalton Trans.*, 2025, **54**, 1370–1376.

42 A. Pfitzner and P. Pohla, *Z. Anorg. Allg. Chem.*, 2009, **635**, 1157–1159.

43 H.-J. Riebe and H.-L. Keller, *Z. Anorg. Allg. Chem.*, 1991, **597**, 151–161.

44 U. Dang, W. Zaheer, W. Zhou, A. Kandel, M. Orr, R. W. Schwenz, G. Laurita, S. Banerjee and R. T. Macaluso, *Chem. Mater.*, 2020, **32**, 7404–7412.

45 (*a*) R. Fakhreddine, A. Ouasri and A. Aatiq, *J. Solid State Chem.*, 2024, **329**, 124439; (*b*) M. A. Azooz, M. A. Ouis and H. A. ElBatal, *J. Non-Cryst. Solids*, 2019, **515**, 82–87;

 

(*c*) M. Ristić, S. Popović and S. Musić, *Mater. Lett.*, 2004, **58**, 2494–2499; (*d*) R. A. Zargar, M. Arora, S. A. Bhat, T. Mearaj, M. A. Manthrammel and M. Shkir, *J. Phys. Chem. Solids*, 2023, **179**, 111390.

46 (*a*) Y. Zeng and D. F. Kelley, *J. Phys. Chem. C*, 2017, **121**, 16657–16664; (*b*) P. A. Giguère and M. Falk, *Spectrochim. Acta*, 1960, **16**, 1–5; (*c*) V. P. Demyakekko, Y. P. Tsyashchenko and E. M. Verlan, *Phys. Status Solidi B*, 1971, **48**, 737–742; (*d*) A. Arndt and M. S. Wickleder, *Eur. J. Inorg. Chem.*, 2007, **2007**, 4335–4339.

47 (*a*) CCDC 2496401: Experimental Crystal Structure Determination, 2025, DOI: 10.25505/fiz.icsd.cc2psq29; (*b*) CCDC 2496402: Experimental Crystal Structure Determination, 2025, DOI: 10.25505/fiz.icsd.cc2psq3b; (*c*) CCDC 2496403: Experimental Crystal Structure Determination, 2025, DOI: 10.25505/fiz.icsd.cc2psq4c.